The Astrophysical Journal, 878:118 (16pp), 2019 June 20 https://doi.org/10.3847/1538-4357/ab204e

Photochemical Hazes in Sub-Neptunian Atmospheres with a Focus on GJ 1214b

Panayotis Lavvas[1], Tommi Koskinen[2], Maria E. Steinrueck[2], Antonio García Muñoz[3], and Adam P. Showman[2]
[1] Groupe de Spectrométrie Moleculaire et Atmosphérique, Université de Reims Champagne Ardenne, Reims, France; panayotis.lavvas@univ-reims.fr
[2] Lunar and Planetary Laboratory, University of Arizona, Tucson, AZ 85721 USA
[3] Zentrum für Astronomie und Astrophysik, Technische Universität Berlin, Berlin, Germany
Received 2019 April 3; revised 2019 April 27; accepted 2019 May 7; published 2019 June 20

Abstract

We study the properties of photochemical hazes in super-Earth/mini-Neptune atmospheres with particular focus on GJ 1214b. We evaluate photochemical haze properties at different metallicities between solar and 10,000× solar. Within the four-order-of-magnitude change in metallicity, we find that the haze precursor mass fluxes change only by a factor of ∼3. This small diversity occurs with a nonmonotonic manner among the different metallicity cases, reflecting the interaction of the main atmospheric gases with the radiation field. Comparison with relative haze yields at different metallicities from laboratory experiments reveals a qualitative similarity to our theoretical calculations and highlights the contributions of different gas precursors. Our haze simulations demonstrate that higher metallicity results in smaller average particle sizes. Metallicities at and above 100× solar with haze formation yields of ∼10% provide enough haze opacity to satisfy transit observations at visible wavelengths and obscure sufficiently the H_2O molecular absorption features between 1.1 and 1.7 μm. However, only the highest-metallicity case considered (10,000× solar) brings the simulated spectra into closer agreement with transit depths at 3.6 and 4.5 μm, indicating a high contribution of CO/CO_2 in GJ 1214b's atmosphere. We also evaluate the impact of aggregate growth in our simulations, in contrast to spherical growth, and find that the two growth modes provide similar transit signatures (for $D_f = 2$), but with different particle size distributions. Finally, we conclude that the simulated haze particles should have major implications for the atmospheric thermal structure and for the properties of condensation clouds.

Key words: planets and satellites: atmospheres – planets and satellites: gaseous planets – planets and satellites: individual (GJ 1214b)

1. Introduction

Super-Earth- and mini-Neptune-size planets constitute a large fraction of the observed exoplanet population and therefore are the subject of intense investigation. Transit observations of such planets reveal a diversity in the depth of spectral features anticipated at near-IR wavelengths from molecular absorption, which is attributed to the presence of suspended particulate matter in their atmospheres (Crossfield & Kreidberg 2017). Such heterogeneous components have been detected also in the atmospheres of the larger hot Jupiters (Sing et al. 2016; Barstow et al. 2017), for which various studies show that photochemical hazes and/or clouds are responsible for the observed signatures.[4] Particularly for the case of HD 189733b, photochemical hazes appear to be better candidates for the interpretation of the observations (Lee et al. 2015; Lavvas & Koskinen 2017; Powell et al. 2018). We explore here the properties of photochemical hazes in the atmospheres of super-Earths/mini-Neptunes using detailed models of atmospheric chemistry and haze microphysics, and we evaluate how such components can help interpret the available observations.

The most well-studied example of such an atmosphere is the case of exoplanet GJ 1214b, for which multiple ground-based and space-borne observations reveal a remarkably flat spectrum extending from visible to IR (see Angerhausen et al. 2017, for an overview of available transit observations). A high-precision evaluation of transit depth at visible wavelengths is prevented by the temporal and spatial inhomogeneities of the GJ 1214 M-dwarf stellar emission (Rackham et al. 2017; Mallonn et al. 2018). Nevertheless, the most accurate constraints at visible from ground-based observations with the Subaru (Narita et al. 2013) and the Large Binocular Telescope (Nascimbeni et al. 2015), in combination with the high-precision *Hubble Space Telescope* (*HST*) observations between 1.1 and 1.7 μm (Kreidberg et al. 2014) and the *Spitzer* measurements at 3.6 and 4.5 μm (Fraine et al. 2013), reveal a quasi-flat spectrum, which restricts the characterization of the atmospheric composition. Simulated transit spectra assuming only gaseous components are inconsistent with the observations even when high solar metallicities are assumed or even pure H_2O/CO_2 atmospheres, hence making the presence of the heterogeneous opacity necessary (Kreidberg et al. 2014). Although the almost featureless transit spectrum of GJ 1214b could be fitted by a planetary body with no substantial atmosphere, such a scenario seems unlikely, as the measured radius and mass of the planet provide a bulk density ($\rho \sim 2$ g cm^{-3}) that is well below the typical rock/metal composition limit. Mass and radius measurements cannot uniquely constrain the composition of the planet; however, thermal evolution models of the planet interior suggest that a few percent of the planet mass should be due to an H/He envelope to explain the measured mass density (Lopez & Fortney 2014; Lozovsky et al. 2018). Thus, the presence of an atmosphere on GJ 1214b is rather probable.

Preliminary studies for the properties of clouds and photochemical hazes in the atmosphere of GJ 1214b suggested that both components can provide a flat spectrum (Morley et al. 2013, 2015). Photochemical hazes are expected to form in the upper atmosphere ($p < 10$ μbars) and coagulate to larger

[4] We consider as hazes the end products of photochemical processes similar to those found in Titan's atmosphere or the soots of combustion/pyrolysis experiments, and as clouds the particles resulting from the condensation of gas-phase molecules.

particles as they sediment to the lower atmosphere, while clouds are expected to form at higher pressures depending on the solar metallicity and temperature conditions. However, the interpretation of the observations with condensates of KCl and ZnS composition (the most likely cloud condensation candidates for the anticipated atmospheric conditions) require high-metallicity conditions (1000× solar), as well as significantly reduced sedimentation velocities for the formed cloud particles. On the contrary, photochemical hazes could explain the observed flatness of the *HST* observations at lower metallicities (50× solar) and without the requirement of reduced sedimentation (Morley et al. 2015).

Studies with general circulation models (GCMs) suggest that atmospheric dynamics could uplift particles in the atmosphere of GJ 1214b (at pressures higher than ∼0.1 mbars), with increasing efficiency as the metallicity increases above solar (Charnay et al. 2015a). Under the assumption that cloud particle sizes are constant with height, a particle radius of 0.5 μm provided the best match to the *HST* observations (Charnay et al. 2015b).

Subsequent investigations focusing on the microphysics of cloud formation (Gao & Benneke 2018) demonstrate that KCl and ZnS clouds could match the available observations only at high metallicities (1000× solar) and under the assumption of strong atmospheric mixing ($K_{ZZ} = 10^{10}$ cm^2 s^{-1}). However, such an efficient mixing is not supported by the GCM results ($K_{ZZ} = 10^7$–10^9 cm^2 s^{-1} from Charnay et al. 2015a), while heterogeneous nucleation on the surface of photochemical hazes, not yet evaluated, could affect the formation of the condensates and modify the resulting cloud particle distribution (Gao & Benneke 2018). A similar qualitative conclusion for the shortcomings of condensates to explain the GJ 1214b transit observations was derived from Ohno & Okuzumi (2018). These results suggest that photochemical hazes could potentially provide a more realistic interpretation.

Previous work on the microphysics of photochemical haze formation on sub-Neptune-size planets demonstrated how the variable degree of haze production can result in different levels of transit spectra flattening (Kawashima & Ikoma 2018) and how aggregate growth can modify the haze properties (Adams et al. 2019). Here we explore further the details of the microphysical description and evaluate the haze properties at different conditions of solar metallicity. We furthermore evaluate the differences between spherical and aggregate growth and discuss the possible implications of the formed hazes on the atmospheric structure. Our work addresses the general properties of photochemical hazes on super-Earth/mini-Neptune atmospheres, and for that reason we compare our results with laboratory experiments simulating the photochemical haze formation at such conditions (He et al. 2018; Hörst et al. 2018).

2. Atmospheric Properties

For the evaluation of the photochemical haze properties we need information on the chemical composition of the atmosphere. We use the 1D nonequilibrium chemistry model we have developed for hot Jupiters (Lavvas et al. 2014) for the investigation of the chemical composition of GJ 1214b. The required inputs for these simulations are the main atmospheric composition, the atmospheric thermal structure and mixing magnitude (K_{ZZ}), and the stellar insolation.

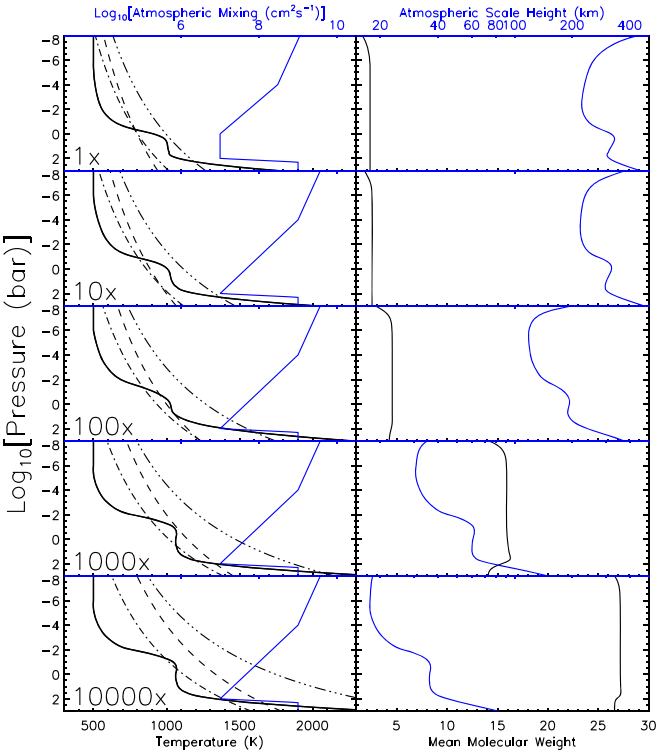

Figure 1. Atmospheric structure assumed for GJ 1214b at different metallicities. Left panels present the thermal structure (black solid lines) based on Gao & Benneke (2018). The dashed, dot-dashed, and triple-dot-dashed lines present the condensation curves for ZnS, KCl, and Na_2S, respectively, assuming thermochemical equilibrium (Morley et al. 2012), while the blue solid lines present the assumed atmospheric mixing profile for each case using input from the GCM models (Charnay et al. 2015a). The right panels present the mean molecular weight (black) and scale height (blue) of the atmosphere based on our disequilibrium chemical composition.

The main composition of GJ 1214b is unknown and a topic of debate (Marley et al. 2013; Kreidberg et al. 2014; Charnay et al. 2015b). Cases from solar metallicity to H_2O- or CO_2-dominated atmospheres have been studied previously, but no definite conclusion could be derived from the available observations owing to the implications of the heterogeneous opacity contribution. As the formation of hazes or clouds depends on species other than the main composition, we need to resort to the approach of a metallicity scaling factor, i.e., evaluate the chemical composition at different scalings of the solar metallicity. Previous studies indicate that a high (1000× solar) metallicity is required to explain the transit spectrum of GJ 1214b, if KCl and ZnS clouds are assumed to be the source of the heterogeneous opacity (Gao & Benneke 2018). However, an explanation based on photochemical aerosols could be less constraining on the metallicity factor. Laboratory studies on the production of photochemical aerosols on super-Earths and mini-Neptunes demonstrate a large diversity in the production rates (Hörst et al. 2018). Thus, we proceed in estimating photochemical haze production rates at 1× , 10×, 100×, 1000×, and 10,000× solar metallicity and discuss how these correlate with the available observational constraints.

For the thermal structure we consider the available profiles reported in the literature for the different metallicity cases we consider (Gao & Benneke 2018), which are based on 1D thermal structure calculations assuming thermochemical equilibrium (Figure 1). For the 10,000× solar metallicity case we

assume the same profile as for the 1000× case based on previous estimates (Moses et al. 2013). GCMs also provide significant information about how these profiles vary around the planet and particularly for the atmospheric regions probed during transit observations (Kataria et al. 2014; Charnay et al. 2015a). The disk-average temperature profiles provided by GCMs are consistent with the 1D calculations; moreover, they demonstrate that center-to-limb temperature changes could be up to ±100 K above 10 mbars. Morley et al. (2015) and Charnay et al. (2015b) demonstrated that heterogeneous opacities of both clouds or hazes can have an impact on the atmospheric thermal structure, resulting in an anti-greenhouse effect that forces stellar visible radiation to be deposited at higher altitudes relative to a clear atmosphere. However, higher-energy photons leading to the haze formation are deposited at much higher altitudes, while, although the detailed pathways of haze formation are not clear at the moment, temperature changes are expected to have a smaller impact on haze properties relative to cloud properties, as long as the temperature remains below the thermal decomposition limit of the haze particles (Lavvas & Koskinen 2017). Photochemical hazes form from a multitude of ion and neutral chemical processes, each with its individual temperature dependence, while condensation depends dominantly on the saturation vapor pressure of the condensing component that has a sharp temperature dependence (Morley et al. 2012). Therefore, we do not consider the implications of temperature changes in our current calculations. Finally, we assume isothermal profiles in the upper atmosphere, although thermospheres are anticipated to form (García Muñoz 2007; Koskinen et al. 2013). However, the chemical complexity anticipated at high-metallicity cases is likely to significantly modify the current understanding of thermospheres based on H_2/H/He atmospheres of hot Jupiters. Thus, a correct evaluation of the thermospheric structure requires an investigation of the coupling between the lower and upper atmosphere over different metallicities and will be addressed separately.

For the 1D atmospheric mixing profile we use results from GCMs at different metallicities (Charnay et al. 2015a). According to these results, the atmospheric mixing is similar for metallicities between 10× and 100× solar, with the mixing magnitude increasing from 10^7 cm^2 s^{-1} at 100 bars to 10^9 cm^2 s^{-1} at 0.1 mbars. For the 1× solar case the mixing profile is weaker by about a factor of 10 relative to the higher-metallicity cases. It is well acknowledged that the eddy mixing magnitude derived by circulation models can only be treated as approximate estimates (Parmentier et al. 2013; Charnay et al. 2015a) subject to uncertainties possibly greater than a factor of 10. Thus, we treat the assumed K_{ZZ} profiles as approximate.

For the stellar flux of GJ 1214 (M4.5, $T_{\rm eff} = 2935$ K, log g(cm s^{-2}) = 5.06) we use input from the MUSCLES database (Figure 2) that combines observations with models of stellar emissions (France et al. 2016; Loyd et al. 2016). Observations with *HST*/STIS allow for the reconstruction of the Lyα emission and provide a flux of 1.3×10^{-14} erg cm^{-2} s^{-1} Å^{-1} reaching the Earth (Youngblood et al. 2016). This value can be used to estimate the EUV emission at broad bins between 100 and 1170 Å (Linsky et al. 2014). The spectral density within each EUV bin is unknown; thus, we assume a solar-type spectral distribution. A similar combination of X-ray observations and simulations provides the spectrum at shorter wavelengths (Fontenla et al. 2016). GJ 1214 is at 14.6 pc, which is sufficiently distant that there exist large uncertainties in the observed spectrum. However, observations of a similar spectral type star, GJ 876 (M5, $T_{\rm eff} = 3062$ K, log g(cm s^{-2}) = 4.93), at 4.7 pc provide an improved accuracy spectrum. Thus, we used the spectral density of GJ 876 to estimate the spectral emission of GJ 1214 for regions where noise dominated the observations, particularly at the Lyα wings and up to ∼3000 Å. At longer wavelengths the MUSCLES spectrum is based on observations with *HST*/STIS and *HST*/COS combined with PHOENIX stellar emission models.

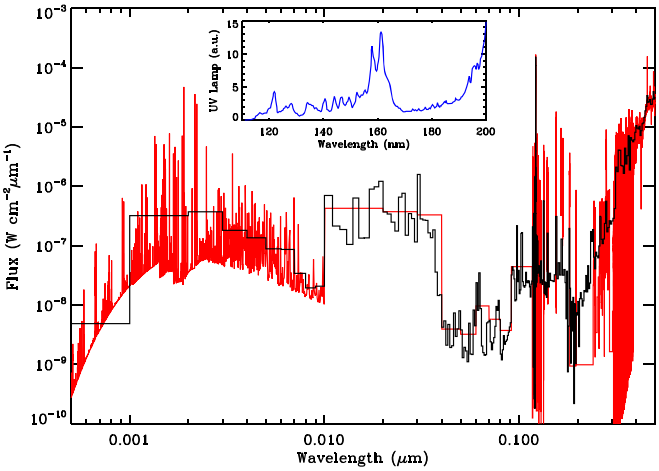

Figure 2. Stellar emission from GJ 1214 assumed in the calculations. The red line shows the high-resolution spectrum based on the MUSCLES database, and the black line depicts the spectrum mapped to the resolution of our model (see text). The inset presents the UV light lamp used for laboratory haze formation for comparison (He et al. 2018).

At the lower boundary (10^3 bars) we consider abundances derived from the CEA thermochemical equilibrium model (McBride et al. 2002). The various metallicity cases we consider result in different main atmospheric compositions that reflect on the mean molecular weight and the corresponding atmospheric viscosity. These parameters are important for the simulation of molecular diffusion and settling velocities of haze particles and are calculated self-consistently as a function of pressure within our model. The mean molecular weight is calculated from our chemical composition calculations, while for the atmospheric viscosity we use the corresponding state method for gas mixtures, taking into account the impact of pressure on the gas viscosity at $p > 10$ bars (Poling et al. 2001).

3. Haze Production

With the above inputs we calculate the chemical composition of GJ 1214b under different metallicity assumptions (Figure 3). Increasing the atmospheric metallicity leads to an increase in the atmospheric mean molecular weight with a concurrent decrease in the atmospheric scale height (Figure 1). The mixing ratios of main atmospheric components in the middle atmosphere (1 mbar) are shown in Table 1 for each metallicity case. The chemistry of hot Neptune atmospheres was investigated in detail in previous studies (e.g., Miller-Ricci Kempton et al. 2012; Moses et al. 2013); thus, we will not dwell on these details here. As these studies demonstrated, as metallicity increases, the abundance of CO/CO_2 progressively dominates over the CH_4 abundance and quenching in the deep atmosphere from atmospheric mixing will affect the relative

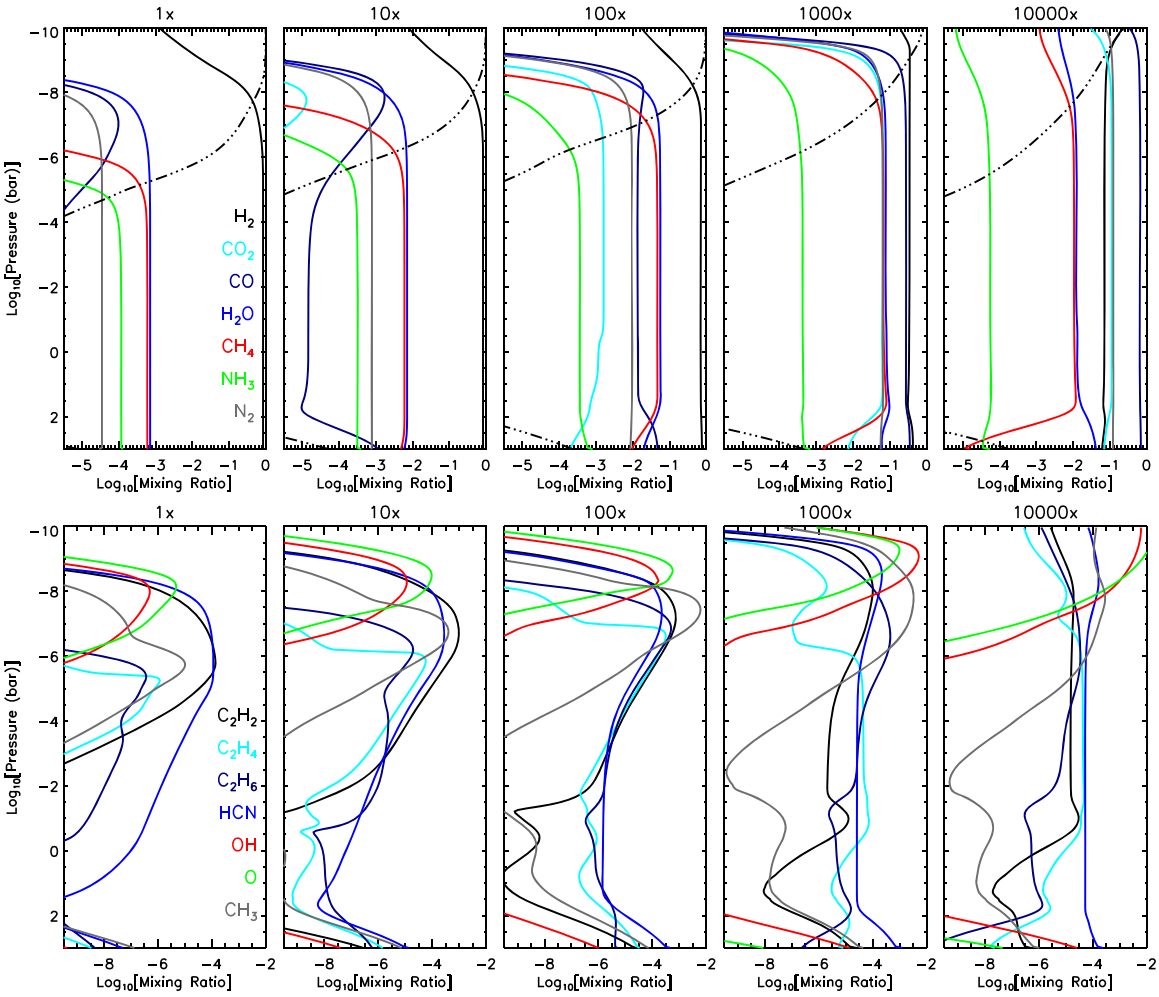

Figure 3. Chemical composition of GJ 1214b for the five metallicity cases and for disk geometry. The top panels present the variation of the main composition (dashed line corresponds to atomic hydrogen), and the bottom panels present the corresponding photochemical products of hydrocarbons and oxygen species.

Table 1
Main Atmospheric Composition at 1 mbar for Different Metallicity Cases According to the Disequilibrium Chemistry Calculations

Species	1×	10×	100×	1000×	10,000×
H_2	0.835	0.822	0.706	0.341	7.08(−2)
He	0.163	0.164	0.167	0.111	2.14(−2)
H_2O	7.13(−4)	7.12(−3)	5.58(−2)	7.77(−2)	1.22(−2)
CH_4	5.94(−4)	6.03(−3)	4.64(−2)	6.74(−2)	1.05(−2)
N_2	3.37(−5)	7.79(−4)	9.52(−3)	6.39(−2)	0.123
NH_3	1.15(−4)	3.26(−4)	3.66(−4)	4.10(−4)	5.39(−5)
CO	5.16(−7)	1.56(−5)	1.35(−2)	0.274	0.651
CO_2	2.11(−10)	2.16(−7)	1.61(−3)	6.43(−2)	0.111

Note Read $a(b)$ as $a \times 10^b$

abundance of CH_4/CO in the upper atmosphere. We consider a nominal value of $K_{ZZ} = 10^9$ cm^2 s^{-1} for the convective region below 100 bars based on Moses et al. (2013). However, a smaller magnitude $K_{ZZ} = 10^7$ cm^2 s^{-1} did not provide different results for all metallicity cases considered.

Our focus here is to evaluate the production rate of soot-type composition photochemical hazes for each case. As in our previous study on hot Jupiters (Lavvas & Koskinen 2017), we estimate the haze mass flux from the photolysis mass fluxes generated by the photodissociation/photoionization of major species in the upper atmosphere ($p < 10\,\mu$bars) multiplied by an approximate yield of haze formation. We consider contributions from the photolysis of CH_4 and N_2 and from their main photochemical products HCN, C_2H_2, and C_2H_4, as well as from NH_3 (see Table 2). A similar approach for the evaluation of photochemical haze mass fluxes was followed in previous studies (Morley et al. 2013; Kawashima & Ikoma 2018), although differences exist on the details of the calculation with other studies focusing on the abundance of various photochemical products and not their photolysis rates.

Hazes based on sulfur composition are also a possible candidate for the temperature conditions of mini-Neptunes/super-Earths (Zahnle et al. 2016; Gao et al. 2017). However, for the solar elemental compositions we consider C to be more abundant than S, and thus likely to provide a higher abundance of soot-type hazes. Moreover, a correct representation of sulfur components requires consideration of cloud formation, as ZnS and Na_2S are likely condensates at the conditions under investigation that will limit the abundance of sulfur-based haze precursors reaching the upper atmosphere. Thus, we focus here on the formation of soot-type haze precursors.

The haze formation yield for HD 189733b was found to range between 0.5% and 10% depending on the atmospheric conditions assumed (Lavvas & Koskinen 2017), while we know that Titan's atmosphere (the most hazy in the solar

Table 2
Photolysis Mass Fluxes (g cm^{-2} s^{-1}) in the Upper Atmosphere of GJ 1214b under Different Assumptions of Solar Metallicity

	Metallicity—Limb					Metallicity—Disk				
Species	1×	10×	100×	1000×	10,000×	1×	10×	100×	1000×	10,000×
CH_4	9.1(−14)	1.1(−12)	2.6(−12)	7.4(−12)	2.9(−12)	1.5(−13)	4.8(−13)	8.9(−12)	7.4(−11)	3.5(−11)
NH_3	3.9(−12)	3.9(−12)	2.8(−12)	1.7(−12)	9.3(−13)	1.3(−11)	2.6(−11)	4.0(−11)	3.4(−11)	6.3(−12)
HCN	2.9(−12)	1.0(−12)	1.1(−13)	8.7(−14)	5.4(−14)	1.6(−11)	6.8(−12)	1.7(−12)	1.9(−12)	2.3(−12)
C_2H_2	1.2(−11)	3.2(−12)	3.4(−13)	8.9(−14)	9.1(−14)	1.0(−10)	8.9(−11)	1.5(−11)	1.3(−12)	5.2(−13)
C_2H_4	4.6(−16)	2.8(−15)	3.1(−15)	1.5(−14)	1.1(−13)	2.6(−13)	1.1(−12)	6.2(−12)	4.8(−13)	1.0(−12)
N_2	1.7(−32)	3.2(−25)	2.6(−23)	5.7(−17)	5.8(−14)	2.0(−20)	6.5(−17)	6.8(−16)	3.8(−14)	1.8(−12)
CO_2	5.8(−16)	4.7(−15)	6.3(−14)	1.3(−12)	2.9(−12)	6.2(−15)	1.0(−13)	2.0(−12)	3.9(−11)	6.9(−11)
CO	3.7(−24)	3.7(−19)	1.2(−17)	1.5(−14)	1.0(−12)	6.9(−17)	2.4(−14)	2.4(−13)	2.8(−12)	3.1(−11)
H_2O	2.6(−11)	2.6(−11)	1.8(−11)	1.4(−11)	3.7(−12)	1.5(−10)	1.5(−10)	1.7(−10)	1.8(−10)	5.2(−11)
Soot(1%)	1.9(−13)	9.2(−14)	5.9(−14)	9.3(−14)	1.2(−13)	1.3(−12)	1.2(−12)	7.2(−13)	1.1(−12)	4.7(−13)

Note. Soot mass fluxes are based on the contributions of CH_4, NH_3, HCN, C_2H_2, C_2H_4, and N_2 scaled by a yield of 1%.

system) has a haze yield of ∼30% (Lavvas et al. 2011a, 2013). Thus, for our preliminary estimates of haze mass fluxes we consider a conservative 1% yield in our tabulated values (see Table 2). We use this estimate only as a tool for comparison among the different metallicity cases, as we evaluate further below what would be the required yield to explain the transit observations. We present chemical composition calculations for both limb (calculated under spherical geometry for tangent rays) and disk (dayside stellar flux for incidence angle of $\mu_0 = 0.5$) geometry conditions to evaluate what would be the difference in the haze production rate at different locations (given the relatively small, ±100 K, horizontal temperature difference suggested by the GCM, we consider the same temperature profile for different geometries). However, we assume that the atmospheric circulation will act toward a homogenization of the particle distribution, although this is something that needs to be evaluated with a coupled model of atmospheric circulation and haze microphysics. Nevertheless, our simulations suggest that significant mass fluxes of photochemical hazes can exist at both limb and disk locations.

With the assumed 1% soot formation yield, haze mass fluxes range between $\sim 2 \times 10^{-14}$ g cm^2 s^{-1} and $\sim 10^{-13}$ g cm^2 s^{-1} for limb geometry and between 7×10^{-13} g cm^2 s^{-1} and 1.3×10^{-12} g cm^2 s^{-1} for disk geometry, for the different metallicity cases. However, increasing the atmospheric metallicity causes changes in the haze production that are not monotonic (Table 2). Using the 100× solar metallicity results as a reference case, we find that lower-metallicity conditions result in higher haze mass fluxes by factors of 1.8 and 1.7 at 1× and 10× solar metallicity, respectively. At 1000× solar metallicity the haze production increases again by a factor of 1.5 before dropping by a factor of 0.65 at 10,000×. The reasons for these variations are due to the changes in the main atmospheric composition at each metallicity case and their implications on the photolysis rates.

At low metallicities the catalytic destruction of H_2 through interaction with OH, produced in the photodissociation of H_2O, leads to the formation of a large abundance of atomic hydrogen in the upper atmosphere (Moses et al. 2011). The latter is a major pathway for the breakup of CH_4 ($H + CH_4 \rightarrow H_2 + CH_3$) and the formation of higher-order hydrocarbons. Therefore, for the solar metallicity case, at pressures lower than 1 μbar methane is lost and C_2-type hydrocarbons are the main hydrocarbon precursors for photochemical haze formation (Figure 3). As metallicity increases to 10× and 100× solar,

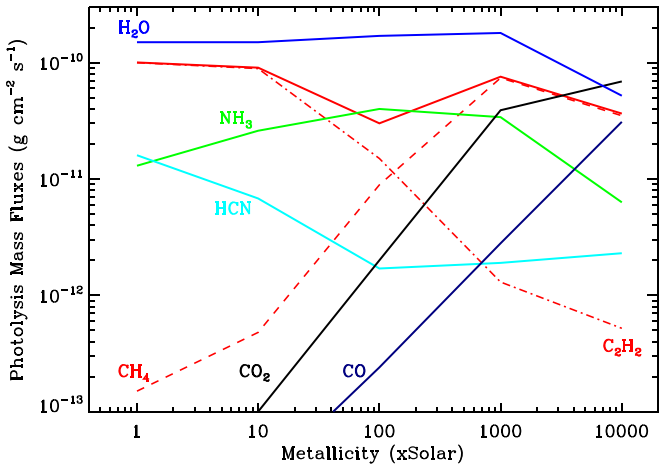

Figure 4. Photolysis mass fluxes from various molecules for different metallicity cases.

the atmospheric pressure where the catalytic destruction of H_2 takes place moves to lower pressures because the abundance of H_2O increases and UV photons are consumed more efficiently in the upper atmosphere, leading to smaller penetration in the atmosphere. Therefore, more methane survives in the upper atmosphere, and the production of higher-order hydrocarbons is reduced. Hence, the photolysis contributions of higher-order hydrocarbons decrease and that of CH_4 increases (Table 2 and Figure 4). Moreover, as metallicity increases, UV photons leading to H_2O photolysis are absorbed by other species as well, leading effectively to a reduction of the atomic hydrogen abundance. This reduction of atomic hydrogen in the upper atmosphere is more prominent for the 1000× and 10,000× solar metallicity cases (Figure 3). At these conditions, the relative contribution of direct photolysis of CH_4 becomes more important and provides the local increase in the haze production rate in the 1000× solar metallicity case. At 10,000× solar metallicity, the CH_4 abundance is reduced, while the opacity of other competing species such as CO and CO_2 is higher, leading to a reduction in methane photolysis (as well as that of other haze precursor species) and an overall decrease of haze production (Figure 4). Below, we further discuss these results in the context of laboratory experiments.

4. Haze Properties

We can now use the above-estimated haze fluxes to simulate the haze particle properties in the atmosphere of GJ 1214b using the haze microphysics model developed for hot Jupiters (Lavvas & Koskinen 2017). In a nutshell, the model solves for the evolution in size (radius) and number density of an initial population of haze embryos, utilizing a bin of particle sizes and solving the continuity equation for each size particle, with contributions from atmospheric mixing, particle sedimentation, and particle coagulation. The initial particle production is described through a Gaussian vertical production profile centered at 1 μbar with a radius of 1 nm. In order to convert the haze mass flux to a production rate of particles, we consider a particle mass density of 1 g cm^{-3}, a typical value assumed for planetary hazes (Lavvas et al. 2010; Rannou et al. 2010), consistent also with laboratory experiments (Hörst & Tolbert 2013). At the lower boundary particles are lost at the rate they arrive.

Particles grow through their mutual collisions (coagulation). There are multiple mechanisms that can affect the particle collision rate (coagulation kernels) such as the particle Brownian motion, gravitational settling, turbulent motions, and convection (Pruppacher & Klett 1978). We have tested all these contributions and found that Brownian motion is the dominant mechanism under the conditions we explore. This conclusion depends on the assumptions made for the particle production profile. For example, assuming that haze particles can form everywhere in the atmosphere would result in a bimodal distribution with small particles locally produced by the chemistry and a larger size component that originates from the sedimentation of particles coagulated at higher altitudes. Such a configuration would enhance contributions from the gravitational settling component of the coagulation kernel because of the different sedimentation velocities of particles found in the two main peaks of the bimodal distribution (Kawashima & Ikoma 2018).

In our simulations we assume that production occurs only in the upper atmosphere; thus, the shape of the particle distribution is monomodal and the gravitational kernel has a minor contribution relative to Brownian motion. Our choice for the particle production profile is based on the current understanding of haze formation in Titan's atmosphere (Lavvas et al. 2011b, 2013). There, haze formation initiates in the upper atmosphere through ion-neutral processes and subsequent growth of formed particles proceeds through heterogeneous processes on their surface. Thus, chemical processes occurring at lower altitudes do not result in the inception of new particles but contribute to the growth of the existing particles. Of course, bimodal particle distributions do exist in planetary atmospheres but are related to different formation mechanisms or dynamical effects from the atmospheric circulation. Therefore, as we consider only a single type of haze in our simulations, we utilize a production profile located in the upper atmosphere.

Our simulations reveal a drastic change in the haze particle properties among the different metallicity cases considered (Figure 5). As metallicity increases, the average particle size below the production region decreases, with the corresponding particle number density increasing. This feature is common for all mass flux cases considered. To interpret this effect, we need to look into the processes defining the particle growth. As discussed above, changing the atmospheric metallicity results in changes in the mean molecular weight and the viscosity of the atmosphere, both increasing with the degree of metallicity. A higher viscosity decreases the particle settling velocity (Lavvas et al. 2010), which would suggest that particle growth should increase with metallicity, as particles have a larger residence time in the atmosphere and are subject to more collisions. Similarly, the coagulation rates increase as the metallicity increases according to our calculations, due to the higher temperature. Moreover, the atmospheric mixing profile (eddy) is similar among the three highest-metallicity cases, implying that its role should be similar. However, the differences in the atmospheric properties among the various cases change the response time for each of the three above processes (settling, coagulation, mixing) and result in the counterintuitive drop of particle growth with metallicity. The change in the characteristic times for particle settling, τ_S, particle mixing, τ_M, and particle collisions, τ_C, among the different atmospheric conditions highlights this effect (Figure 6). These times are calculated from

$$\tau_S = \frac{H}{\langle v_p \rangle}, \quad \tau_M = \frac{H^2}{K_{ZZ}}, \quad \tau_C = \left\langle \frac{n_p}{\partial n_p / \partial t}, \right\rangle \tag{1}$$

with brackets corresponding to averaging over the particle size distribution. At solar metallicity, particle collisions have the smallest characteristic time, leading to a rapid growth of the average particle size. Only below ~1 bar, atmospheric mixing due to the strong inversion assumed in the eddy profile dominates over collisions, and the particles are rapidly transferred toward the lower boundary, thus explaining the rapid drop on the particle number density observed for all metallicity cases at that location. At higher metallicities, as the mean molecular weight increases and the atmospheric scale height decreases, the characteristic time for atmospheric mixing in the upper atmosphere decreases. Thus, even if the eddy mixing profile is the same for the 10×, 100×, and 1000× solar metallicity cases, the characteristic time of atmospheric mixing becomes progressively smaller and particles are subject to fewer collisions. Thus, the rate of increase in the average particle size becomes progressively smaller with increasing metallicity (Figure 5). Our simulations show that at 1 mbar and for a haze mass flux of 10^{-12} g cm^{-2} s^{-1} the average particle size decreases from ~75 to ~3 nm between the 1× and the 10,000× solar metallicity cases, while the corresponding particle number density increases from ~50 to $\sim 7 \times 10^4$ cm^{-3}.

Within each metallicity case, increasing the mass flux results in larger particle sizes as already anticipated from our previous study on hot Jupiters (Lavvas & Koskinen 2017). When comparing solar metallicity simulations, the current results are close to those derived for hot Jupiters at similar conditions of mass flux and atmospheric mixing, as long as the mixing efficiency is large enough to compensate for the reduction in the characteristic sedimentation velocity of the particles in hot Jupiters due to their stronger gravitational field. Moreover, due to the cooler thermal structure, particle thermal decomposition is not efficient in the pressure range under investigation for GJ 1214b.

For these calculations we assumed that particles are not charged and thus there is no impedance in their coagulation. However, particle charging will occur in the atmosphere as a result of photoionization or interaction with charge carriers

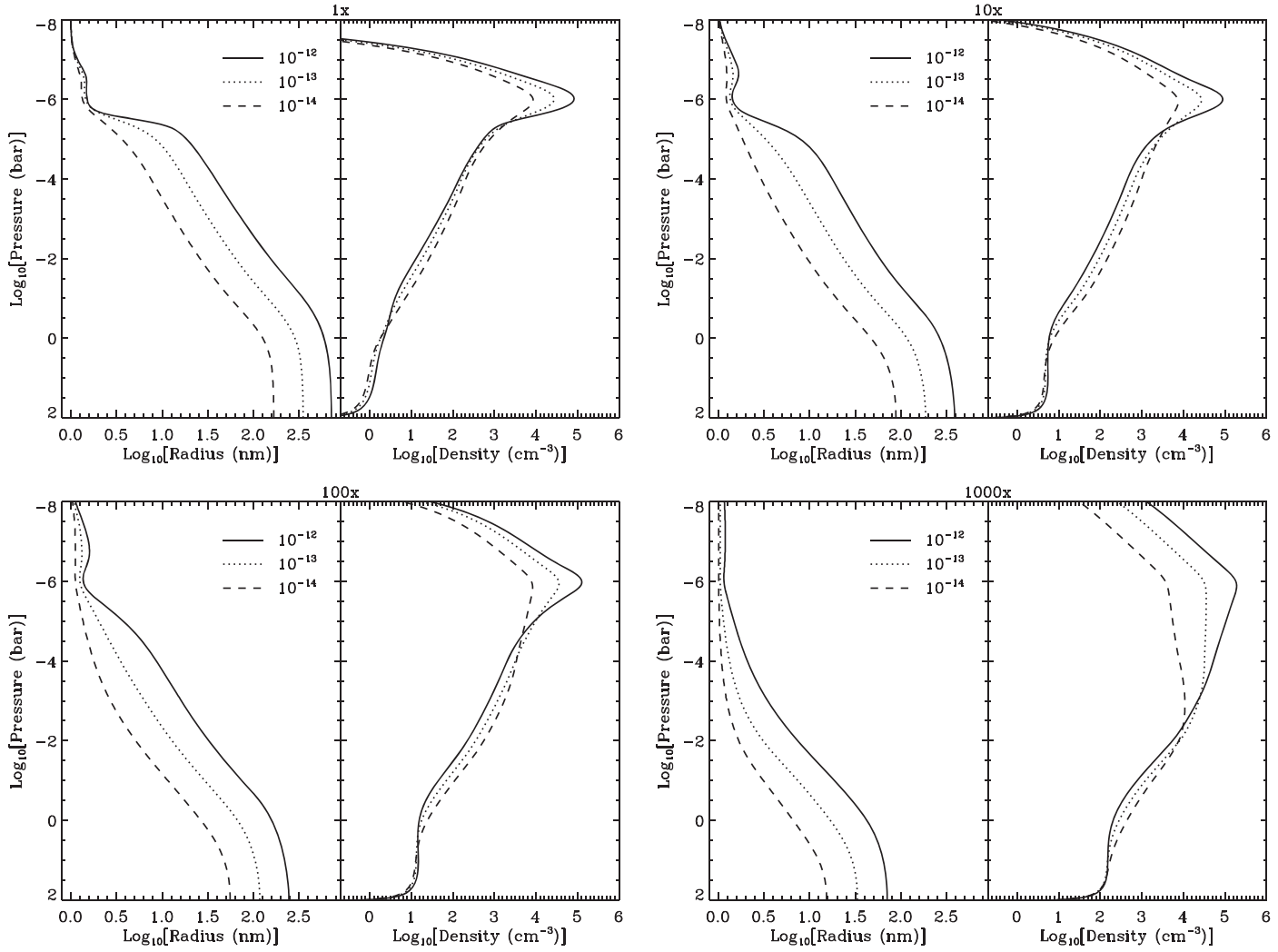

Figure 5. Average radius and corresponding number density of haze particles in the atmosphere of GJ 1214b, under different assumptions of haze mass flux and metallicity.

such as electrons and ions. Charge effects become more efficient with increasing particle size, as larger particles allow for a higher number of accumulated charges. A detailed treatment of the particles' charge distribution is beyond the scope of this evaluation. However, we evaluated the impact of different charge densities, χ, on the particle size distribution (Lavvas & Koskinen 2017). Our calculations suggest that for typical χ values considered for photochemical hazes (10–30 e^-/μm), particle distributions are affected mainly at pressures greater than 100 mbars, with the average particle size reducing by factors between ~1.1 and 1.6 for 10 and 30 e^-/μm, respectively, relative to the $\chi = 0$ case at solar metallicity (and mass flux of 10^{-12} g cm^{-2} s^{-1}). However, as the average particle size decreases for higher metallicities, charge effects becomes less important, and at 10,000× solar metallicity they have no impact on the particle size distribution for the above χ values. At the pressure range where charge effects are important, haze particles are likely to be lost owing to condensation (see Figure 1 and discussion below); thus, the particle size distribution will be drastically different. Therefore, we will not discuss this effect further here.

5. Transit Spectra

Our simulated transit spectra for different metallicities reveal the impact of the photochemical haze distributions for each case (Figure 7). Due to the degeneracy between planet radius and corresponding pressure for gaseous planets, we need to assume a reference planetary radius to which all simulations are referred (Lavvas & Koskinen 2017). For our simulated spectra we used the 3.6 μm *Spitzer* observation as the reference point (Fraine et al. 2013), as these observations have small uncertainty and we wish to utilize the measurements at shorter wavelengths for the characterization of the haze properties.

The simulated spectra of clear atmospheres demonstrate how the increase in metallicity makes the transit signatures more shallow owing to the drop of the atmospheric scale height. However, even for the highest-metallicity case considered (10,000× solar) a clear atmosphere (considering only the gas-phase abundances) cannot reproduce the observed flatness, as the transit depth at visible is always short of the observations (Nascimbeni et al. 2015), while the H_2O bands provide much deeper troughs than the observations reveal in the near-IR (Kreidberg et al. 2014). Thus, a heterogeneous opacity is necessary to explain the observations.

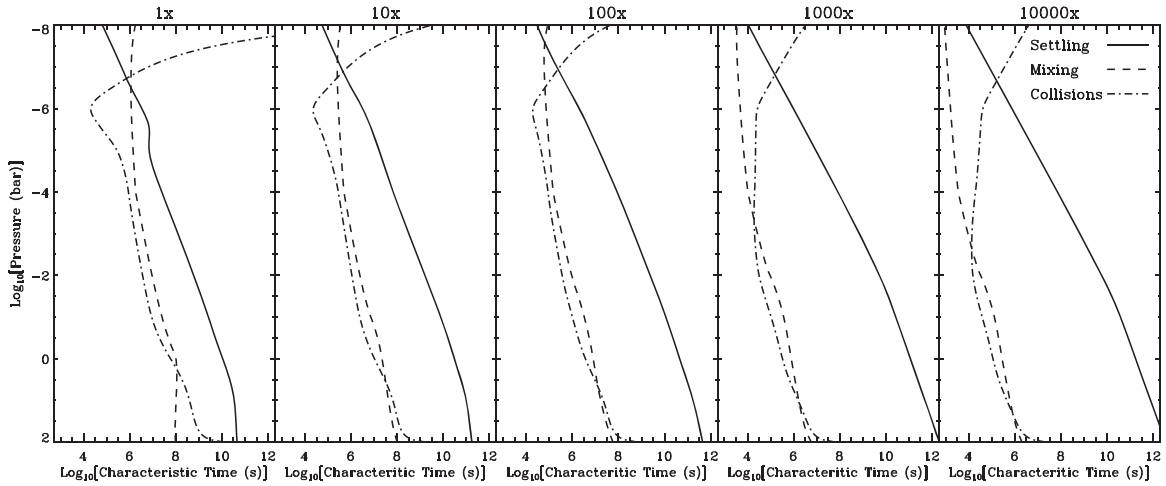

Figure 6. Characteristic times for settling, mixing, and coagulation (collisions) for the haze particles of GJ 1214b's atmosphere, for different metallicity cases. The haze mass flux is 10^{-13} g cm^{-2} s^{-1}.

Even if low-metallicity cases do not apply to the atmosphere of GJ 1214b, it is useful to highlight the variation of photochemical haze contribution in the observed spectra for consideration in other planetary cases (Crossfield & Kreidberg 2017). At low metallicities, we saw that the atmospheric scale height is large and mixing timescales are low. Thus, haze particles remain at high altitudes with a large abundance and affect significantly the observed transit spectrum at visible wavelengths, even for very low formation yields ($\sim$0.01% for solar metallicity). As metallicity increases, haze opacity in the upper atmosphere decreases, and for a given haze mass flux the pressure probed during transit moves to higher pressures, since photons can penetrate to deeper layers before haze opacity sufficiently increases to block them (Figure 7). For metallicities at and above 100$\times$ solar, a higher haze formation yield needs to be considered in order to bring the simulated spectra close to the observations. A mass flux of the order 10^{-11} g cm^{-2} s^{-1} provides enough opacity in the visible/near-IR to bring the transit spectrum close to the observations. Such a mass flux suggests a haze formation yield of $\sim$10%–20%. However, as we discuss below, contributions from the photolysis of CO/CO_2 could further enhance the haze mass fluxes, in which case a common $\sim$10% for all high-metallicity cases (above 100$\times$ solar) is sufficient to reproduce the observations.

The observed variation of the transit signature among the two *Spitzer* wavelengths, with the transit depth at 4.5 μm higher than at 3.6 μm by $\sim 4\sigma$, suggests that the higher-metallicity end provides the most representative case among those we consider. In our simulations the increase of CO_2 with increasing metallicity reduces the high contrast between the two bands characteristic of low metallicities and brings them closer to the observed behavior at the 10,000$\times$ solar metallicity case. However, even in this case the simulated ratio of transit at the two wavelength bands is not as close as in the observations, suggesting a further enhancement of CO_2 relative to our calculations.

6. Aggregation

So far we assumed that the haze particles grow as spheres. However, aggregation is a physical consequence of solid particle collisions and is likely to occur for the photochemical hazes we consider here. The onset of aggregate formation occurs when mass addition from the gas phase is negligible compared to the mass added through particle collisions. Vice versa, aggregated particles can grow to a spherical shape if the rate of mass addition by gas deposition (heterogeneous processes) is larger than the rate of mass addition due to coagulation, as demonstrated by experiments and simulations (see Lavvas et al. 2011b, and references therein). Such a shape transition is more feasible when particles have a small size, which is why in our previous study of hot Jupiters we considered only spherical growth. Our simulations suggested that the particle size required to match the transit observations of HD 189733b was of the order of a few nanometers, at which size heterogeneous reactions on the particle surface could readily preserve the sphericity of the particles (Lavvas et al. 2011b; Lavvas & Koskinen 2017). On the contrary, our simulations for GJ 1214b, depending on the assumed metallicity, show that larger particle sizes can possibly affect the transit signature. Larger particles in the upper atmosphere are mainly characteristic of low-metallicity conditions, which appears inconsistent with the near-IR transit signatures. However, aggregate particles have different optical and microphysical properties (in terms of their collisional efficiency and aerodynamic drag) from spherical particles, which may result in a different transit depth signature. For example, an aggregate particle has a larger cross section than the same mass spherical equivalent, resulting in higher coagulation rates and hence faster particle growth. Moreover, aggregates with structures typical of those found in Titan's atmosphere ($D_f = 2$; see below) have sedimentation velocities representative of their primary particle size in the free molecular regime (Cabane et al. 1993; Lavvas et al. 2010; Rannou et al. 2010). Thus, the rapid growth of aggregates will not be limited by an increase of their settling in the upper atmosphere, as would be the case for spherical particles. Therefore, we explore here the haze properties for aggregates.

An overview of the properties of aggregate particles can be found in previous studies on Titan's atmosphere, where hazes are known to be of aggregate structure (see review by West et al. 2014, and references therein). In a nutshell, particle aggregation under atmospheric conditions results in particle structures that are characterized as fractals with a fractal dimension, D_f. This means that the distribution of primary particles composing the aggregate structure satisfies a

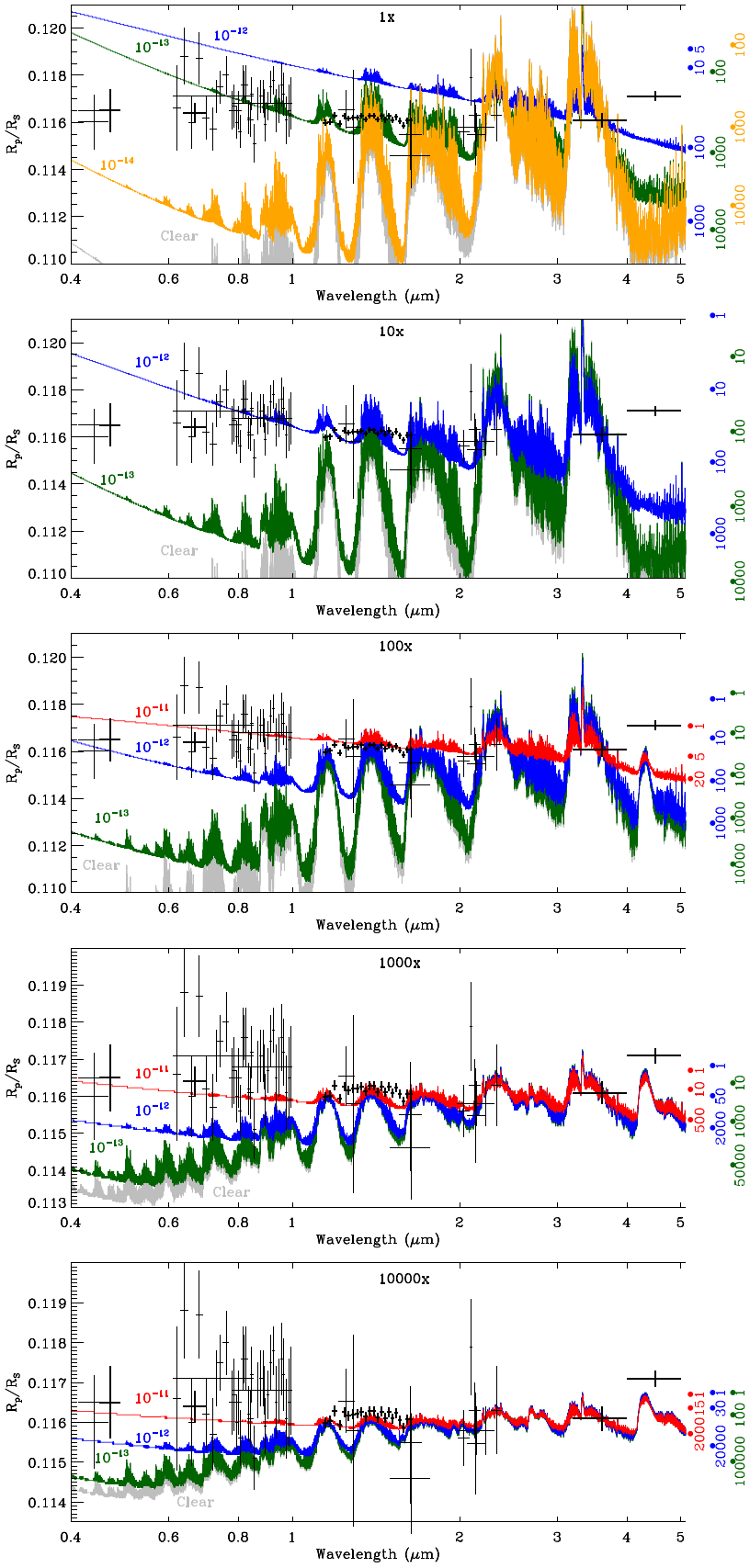

Figure 7. Observed (black crosses) and simulated (color lines) transit depth of GJ 1214b. Each panel presents a different metallicity case and each color line a variation on the assumed haze mass flux. The points and associated numbers on the right of each panel present the pressure (in μbars) probed at each wavelength. Note that for clarity the pressure range plotted in each panel is different.

relationship $N_p \sim R_f^{D_f}$, with N_p the number of primary particles and R_f the fractal radius of the aggregate (see Lavvas et al. 2010, and references therein). The value of D_f depends on the conditions at which the aggregate is formed. Theoretical studies (see Cabane et al. 1993, and references therein) demonstrate that during ballistic collisions (when the particle mean free path, λ_p, is much larger than R_f) collisions between primary particles and aggregates lead to $D_f \sim 3$, while collisions between aggregates result in $D_f \sim 2$. At the opposite extreme of the continuous regime ($\lambda_p \ll R_f$) the corresponding fractal dimension limits are $D_f \sim 2.5$ and $D_f \sim 1.75$ for primary particle–aggregate and aggregate–aggregate collisions, respectively. These pure microphysical cases can be further modified by heterogeneous processes on the surface of the particles, as discussed above, which may result in a further increase of D_f.

The combined contributions of photochemistry that leads to the inception of particles, heterogeneous chemistry on the particle surface, and particle collisions define the primary particle radius (Lavvas et al. 2011b). Typical values of primary particle radii from atmospheres of our solar system are of the order of tens of nanometers, e.g., 10 nm for the aggregates in Pluto's atmosphere (Gladstone et al. 2016) and 40 nm for Titan's haze (Tomasko et al. 2009). As we do not yet have a clear picture of this complex mechanism for the conditions under investigation, we treat the primary particle radius as a free parameter and evaluate results for primary particle radii between 10 and 50 nm. Moreover, we assume that $D_f = 2$ below the particle production region. This is a valid approach, since below the production region where aggregate–aggregate collisions will dominate ballistic conditions apply. We estimate that the continuous growth regime applies at pressures higher than ~0.1 bars, where $\lambda_p = 0.1 \times R_f$ for our calculated size distributions. There, the simulated particles would already be consumed in the formation of clouds; thus, modifying D_f will not provide a physically improved solution. Adams et al. (2019) assumed a $D_f = 2.4$ in their simulations of aggregate growth, considering that restructuring of the aggregates due to motion of the primary particles within each aggregate and due to condensation is possible. Although these processes are possible, we choose $D_f = 2$ in our simulations, as this value has reproduced well the haze properties in Titan's atmosphere (Lavvas et al. 2010; Rannou et al. 2010), while a better understanding of the role of condensation on the fractal dimension requires a coupled description with the condensing gases. Further below we discuss the role of hazes in condensation, but we choose first to simulate here the pure haze case and demonstrate the possible differences inflicted by the choice of fractal dimension.

Compared to results from the previous simulations of spherical growth, where the produced particles were assumed to have a radius of 1 nm, the aggregate simulations provide much smaller particle number densities in the upper atmosphere, as for the same production rate the mass is distributed into larger particles (Figure 8). As the collision rates for aggregates are larger than the corresponding rates for the same mass spheres, there is a fast growth of the particles with a corresponding decrease in the particle number density. This is evident when comparing the average radius during spherical growth (blue lines) with the average radius of the equivalent spherical mass of the aggregate distribution (red lines). The latter is larger than the former owing to the porosity of the aggregates that forces the same mass to be distributed over a

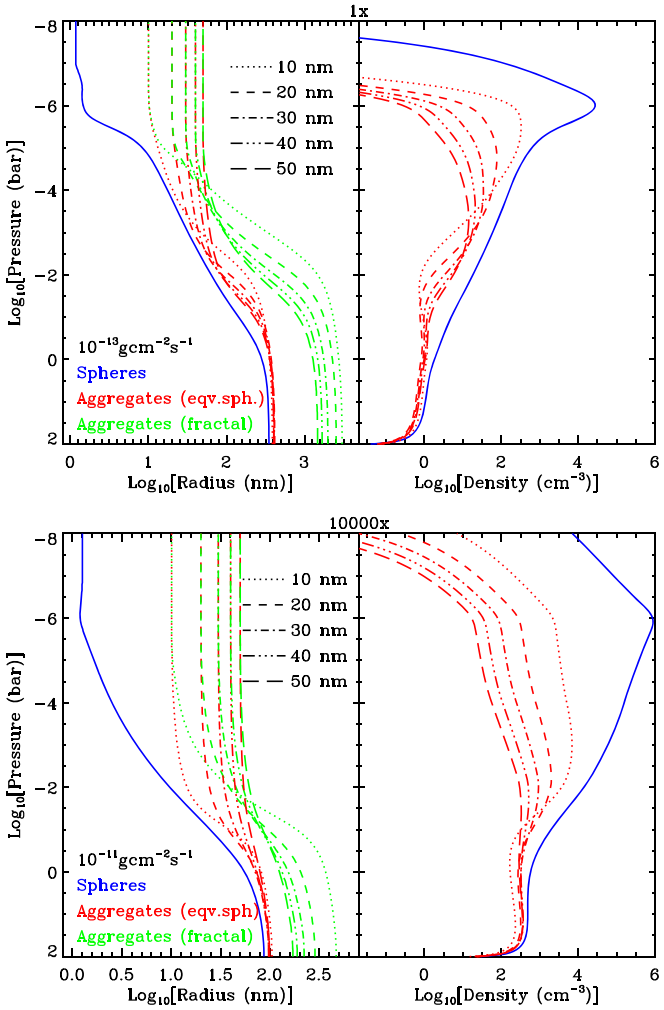

Figure 8. Comparison of spherical (blue) and aggregate (red and green) growth of haze particles for 1× and 10,000× metallicity cases. Each broken line corresponds to a different primary particle radius. For aggregates the red lines correspond to the average radius of the equivalent mass spherical particle and the green lines to the fractal structure average radius. The corresponding average particle density is shown in the right panels (it does not depend on the radius-type averaging). Note that the assumed mass fluxes for each metallicity case are different and correspond to those providing results close to the observed transit spectra.

bigger particle volume. Note that all cases reach a common limiting value of average size and number density in the deep atmosphere. This limit exists because, for a given mass flux, collisions limit the particle number density; thus, once the abundance of particles is sufficiently reduced, the growth terminates. However, when considering the collisional and optical cross section of the aggregates, we need to evaluate the effective cross section of the fractal structures (green lines). These demonstrate the drastically different effect the aggregation has on the particle properties, with average particle radii being up to an order of magnitude larger than the corresponding particles under spherical growth.

Although the aggregate growth picture is qualitatively similar to that of spherical growth, the involved rates are different (Figure 9). The particle growth is faster for smaller primary particle radii owing to the larger number density of particles available for collisions. For larger primary particles, the sedimentation velocity of the formed particles increases and also becomes a limiting factor for the collisional growth in the

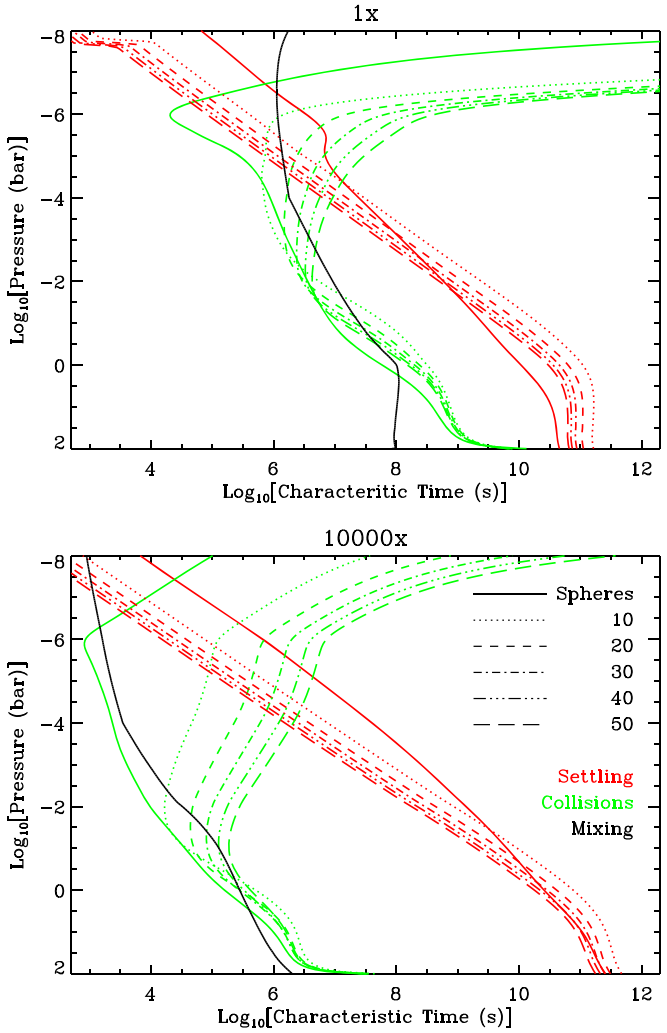

Figure 9. Comparison of characteristic times for settling (red), collisions (green), and sedimentation (black) for spheres and aggregates of different primary particle radius (shown in nm).

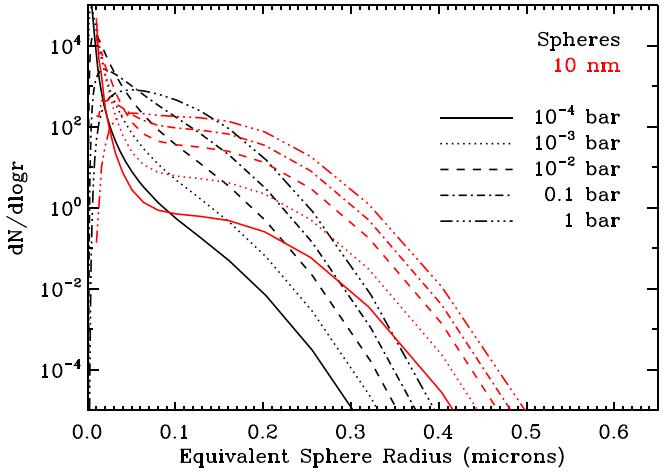

Figure 10. Particle size distribution for spherical (black) and aggregate growth (red, 10 nm primary particles) for the 10,000× solar metallicity case and for a haze mass flux of 10^{-11} g cm^{-2} s^{-1}. Each line style corresponds to a different pressure level as shown.

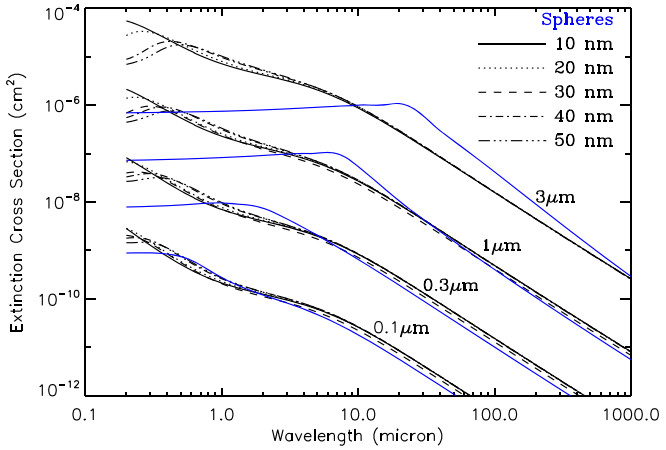

Figure 11. Wavelength dependence of the extinction cross section of aggregate particles with different primary particle radii (black lines) compared to the extinction by the same mass spherical particle (blue lines). Four different cases of particle sizes are presented, ranging from 0.1 to 3 μm for the equivalent mass–radius.

upper atmosphere, as particles rapidly sediment to the lower atmosphere. For all cases, aggregation results in larger particle radii with corresponding smaller particle number densities compared to the spherical growth case, for the parts of the atmosphere affecting the transit depth. Moreover, the particle size distribution for aggregates is broader than the corresponding distribution for spherical particles (Figure 10). This effect is a demonstration of the common sedimentation velocity of the particles that makes settling differentiation at a given pressure level less efficient compared to spherical particles.

We calculate the optical properties in our aggregate particle distribution utilizing the analytical approach based on the T-matrix model results (Tomasko et al. 2008) assuming a soot composition refractive index (Lavvas & Koskinen 2017). The optical properties of an aggregate particle are different from those of the same mass spherical particle and demonstrate higher extinction at UV and lower at IR (see Figure 11), with the transition point between these two limits depending on the size and number of primary particles composing the aggregate. A clear characteristic of aggregates is that they result in a sharper wavelength dependence at short wavelengths in their extinction properties, relative to that of equivalent mass spheres. However, when comparing small spherical particles with larger aggregates, i.e., the impact of aggregation on our simulations, although the absolute cross sections are much larger for the aggregates, the wavelength dependence of cross section for the two particle types is similar. Thus, when included in our calculations (Figure 12), we find that aggregate-based transit spectra are very close to those of the spherical particles. Remember that we consider the 3.5 μm observations as a reference point for the alignment of the pressure scale (see above and also in Lavvas & Koskinen 2017). Thus, although aggregates provide a higher opacity, their similar spectral signature with smaller spherical particles provides the same transit signature. This is a different conclusion from what was recently derived by Adams et al. (2019). Based on the results presented by the latter authors, their calculations for the wavelength dependence of aggregate extinction suggest a far more flat wavelength behavior, similar to what is anticipated for large spherical particles (Figure 11). Their calculations are based on a different approach (Rannou et al. 1997), which, however, provides the same general characteristics for $D_f = 2$, with an increase of extinction at UV and decrease at IR relative to the equivalent mass spherical particle. On the other hand,

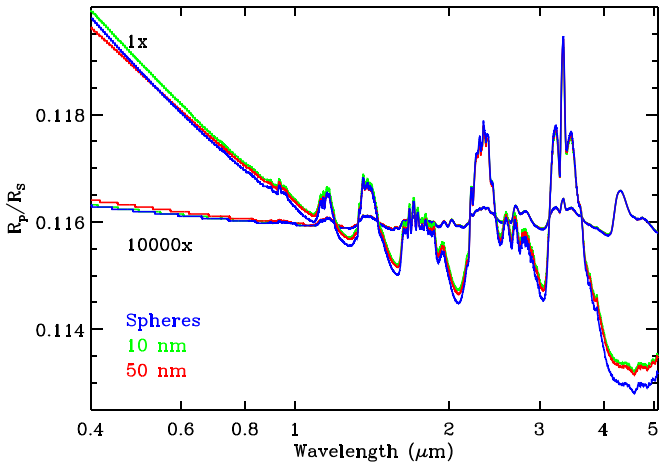

Figure 12. Comparison of transit spectra for spherical and aggregate shape haze simulations (see Figure 8) for the 1× and 10,000× solar metallicity cases. Note that spectra are smoothed for clarity.

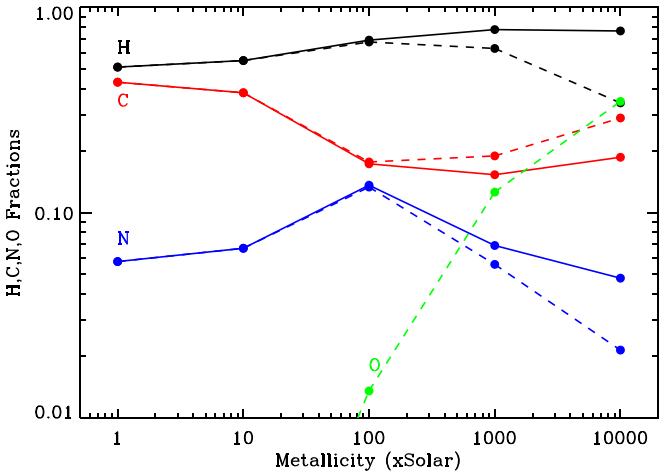

Figure 13. Fractional abundance of different elements in the photolysis mass fluxes presented in Table 2. Solid lines present the case of nominal haze production by photolysis of CH_4, N_2, and their main photochemical products, while dashed lines consider the additional contributions from CO and CO_2 photolysis.

Adams et al. (2019) assume a fractal dimension of 2.4 in their calculations, which brings the wavelength dependence of the haze opacity closer to that of spherical particles, i.e., flatter (see Figure 3 in Rannou et al. 2016),[5] and is the reason for the different conclusion derived by these authors.

This similarity between transit spectra for spheres and aggregates demonstrates that extinction measurements cannot uniquely constrain the size/shape of particles. In other words, transit observations can be equally well fitted by spherical or aggregate structure particles. Instead, polarization measurements (Tomasko et al. 2009; García Muñoz 2018) or observations at different planetary phases (García Muñoz et al. 2017; Seignovert et al. 2017) are required for a better characterization of the particle shape. In our transit depth calculations we did not consider the possible contribution of forward scattering from the particles (Robinson et al. 2017; García Muñoz & Cabrera 2018). This contribution will be more important for the aggregate particles that are known to demonstrate a strong forward peak (Lavvas et al. 2010). However, recent evaluations of this effect suggest that it reduces the transit depth by less than a scale height (García Muñoz & Cabrera 2018). Thus, we did not consider it here.

7. Discussion

Our simulated haze production rates demonstrate that although the metallicity conditions change by four orders of magnitude, the difference in the haze mass fluxes is only a factor of ∼3 between the two extreme cases of solar and 10,000× solar metallicity. This is a clear demonstration of the fact that photochemical products are dominantly photon limited, as long as the abundance of precursors is not critically affected by their photolysis. For example, Pluto and Triton have very similar atmospheres of CH_4/N_2 composition. Yet, the combination of higher-energy input and lower CH_4 abundance on Triton relative to Pluto results in a major destruction of Triton's atmospheric CH_4 above ∼200 km altitude (Krasnopolsky & Cruikshank 1995) that limits the production of heterogeneous components close to this moon's surface, contrary to Pluto, where hazes are observed at high altitudes (Gladstone et al. 2016). Thus, with the exception of such extreme cases, metallicity changes should not induce major changes to the precursor mass fluxes, and thereby to the haze production rates.

Nevertheless, metallicity changes can impose chemical composition changes with a secondary impact on the particle composition. The relative contributions of H, C, and N in the photolysis of precursors (Figure 13) demonstrate this dependence on the assumed metallicity. Under the nominal soot precursors (i.e., photolysis of CH_4, N_2, and their main photochemical products; see above), increasing the metallicity above solar and up to 100× solar results in a decrease of the available C and an increase of N, while at higher metallicities the C fraction remains approximately constant while N decreases. These fractions only correspond to the composition characteristics of the precursor's photolysis mass fluxes and do not necessarily reflect the composition of the soot particles. However, they are indicative of what can be anticipated of the hazes.

The simulated haze production rates at high-metallicity conditions are particularly interesting because they can be compared to experimental retrievals of photochemical haze formation at similar conditions. Laboratory investigations for the production of photochemical hazes in super-Earths/mini-Neptunes show production at all metallicity conditions studied (100×, 1000×, 10,000×), with production rates varying according to the energy source and the temperature conditions (He et al. 2018; Hörst et al. 2018). For experiments performed under UV irradiation, which are more relevant to the photochemically produced hazes studied here, particle production for each metallicity case dropped when temperature increased from 400 to 600 K (He et al. 2018). For each temperature, particle production among different metallicity cases showed a different dependence (Figure 14): at 400 K the relative haze production was slightly higher at 1000× compared to 100× solar metallicity and dropped by a factor of 2 at 10,000×, while at 600 K a monotonic increase was observed with increasing metallicity.

A direct comparison with these experimental results is not straightforward, as we can compare only relative yields among the different metallicity cases considered. Moreover, our

[5] Note that in Figure 2(a) of Rannou et al. (2016) the assignments of D_f are mistakenly inverted.

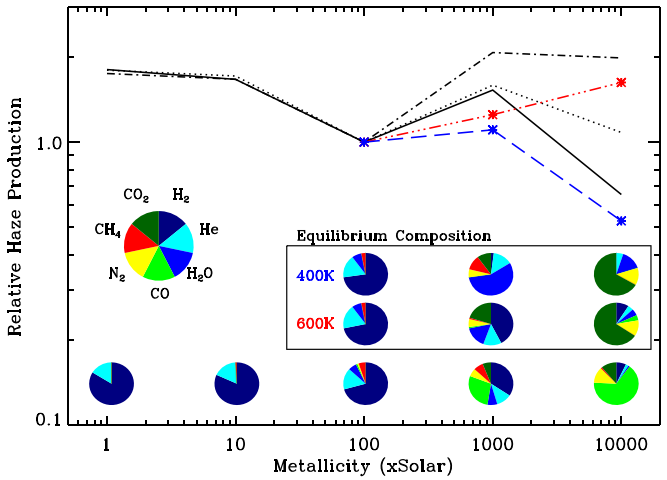

Figure 14. Relative haze production from simulations (lines) and laboratory experiments (asterisks) at different metallicities (see text). The black line corresponds to the nominal haze precursors (CH_4 and N_2 photochemical products), while the dotted and dot-dashed lines present additional contributions from the photolysis of CO and CO_2, respectively. All curves are normalized to the 100× solar metallicity case. Pie charts at the bottom present the main gas composition for each case.

simulations are representative of the photochemistry occurring at 500 K in the upper atmosphere of GJ 1214b, where the main atmospheric composition is defined by disequilibrium chemistry (Table 1). On the contrary, the experiments performed at the bracketing 400 and 600 K temperature cases had a main gas composition based on thermochemical equilibrium conditions at 1 mbar pressure (He et al. 2018). Nevertheless, our calculated compositions at 100× and 1000× solar metallicity cases are not very different from those of the experiments (see pie charts in Figure 14). At 100× the disequilibrium CH_4 mixing ratio at 500 K (4.6%) is very close to the experimental value used (4.5% at 400 K and 3.4% at 600 K), and the rest of the main composition is similar between our calculations and the experiments, with the only difference being a small contribution (∼1%) of N_2 in our calculations. At 1000× our CH_4 mixing ratio (6.7%) is in between the two equilibrium abundances (11% at 400 K and 1.7% at 600 K). However, the main gas composition in our simulation is based on H_2 (34%) and CO (27%), while for the experiments the main equilibrium composition changes from H_2O (56%) at 400 K to H_2 (42%) and CO_2 (20%) at 600 K. These changes in the main composition of our simulations occur as a result of quenching in the lower atmosphere by the atmospheric mixing (Figure 3). However, the relative contributions of C–H/C–O species are qualitatively similar between our calculations (6.7/33.8) and the experiments (11/10 at 400 K and 1.7/21.9 at 600 K). This picture drastically changes for the 10,000× solar metallicity case, for which the disequilibrium composition includes ∼1% CH_4, while for the equilibrium conditions methane is a minor species not included in the experimental gas mixture. In addition, the main composition in the disequilibrium conditions is based on CO (65%) with contributions from CO_2 (11%) and N_2 (12%), while at equilibrium CO_2 (67%) is the main gas component (Figure 14). There are also differences in the spectral density of the UV light used in the experiment and that of GJ 1214, which impose further reasons for differentiation in the results. Lyα (121.6 nm) dominates the UV stellar spectrum, while the laboratory UV lamp has a stronger output near 160 and 230 nm relative to 121.6 nm. Notwithstanding these differences between experimental and theoretical derivations, we can identify some qualitative similarities.

For both experiments and theoretical calculations increasing the metallicity from 100× to 1000× solar results in higher haze production (Figure 14). Although the photolysis mass fluxes from the disequilibrium chemistry suggest a stronger increase than the experimental results at 400 and 600 K, qualitatively both theory and experiments provide the same picture, and the observed differences are likely related to the differences in the gas abundances and UV spectral density identified above. For example, at 1000× solar metallicity H_2O and CO_2 have significant abundances in the experimental mixtures at 400 and 600 K, respectively, which are replaced by H_2 and CO in our calculations. The latter two gases do not intervene in the photolysis of hydrocarbons, contrary to the former two gases that have major absorption bands at UV wavelengths and will screen the photolysis of methane and other hydrocarbons, resulting in smaller haze production.

At 10,000× solar metallicity, our calculations show a clear decrease in the haze production that is consistent with the experimental results at 400 K. However, our estimated haze production is based only on hydrocarbons and N-containing species (N_2, NH_3, HCN), while the experimental conditions do not include any CH_4. This characteristic suggests that formation of photochemical hazes from the photolysis of CO/CO_2 is also possible (He et al. 2018; Hörst et al. 2018). If we consider the possible contribution of carbon from the photolysis of CO in the theoretical haze mass flux estimates (dotted curve in Figure 14), we derive a higher haze production, which becomes even higher if we also consider the photolysis of CO_2 (dot-dashed curve). In addition, the fractional C-abundance increases with these contributions at high-metallicity cases, suggesting that the hazes become more carbonaceous at these conditions (Figure 13).

The CO/CO_2 contributions bring the relative haze production close to the metallicity behavior seen at 600 K, but they also increase further the production at the 1000× solar metallicity case. A naive interpretation of the experimental results at the two temperatures would suggest that the relative contribution of CO/CO_2-produced hazes is higher at 600 K than at 400 K. Although such a behavior may partially contribute to the observed behavior, these relative yields have to be examined through the prism of the main gas composition. The main difference of the gas composition at the two temperatures studied in the laboratory experiments at 10,000× solar metallicity is that at 400 K there is ∼3× more H_2O than at the equilibrium composition at 600 K, which could impose a significant reduction on the haze formation, again through photolysis screening of other species, as well as by oxidizing reactions. In our corresponding disequilibrium simulations the H_2O abundance (1.2%) is closer to the 600 K case, for which we get a similar relative production.

In addition, differences in the chemical rates imposed by the different temperature conditions could further affect the haze production. We note that experimental and theoretical results correspond to the different steps of the photochemical haze production: the experiments measure the abundance of the formed haze particles, i.e., the end products of the photochemistry, while our theoretical estimates are based on the first steps of the atmospheric photochemistry. These two extremes are related by the haze formation yield. The qualitative consistency between our theoretical simulations and the

experimental results verify the appropriateness of this approach. However, the comparison also demonstrates that utilizing the photolysis mass fluxes provides a more robust estimation of the haze production, instead of scalings based on the abundances of individual precursors. This is readily demonstrated by observing that abundances across metallicity cases demonstrate a monotonic variation (e.g., CH_4 and HCN in Figure 3) that would result in monotonic haze production yields across metallicities, inconsistent with the experimental results.

We highlight that the above discussion applies only to the relative production yields. The experiments reveal that absolute yields increase with decreasing temperature for the 100× and 1000× metallicity cases, while the opposite behavior was observed for the 10,000× solar metallicity case (He et al. 2018). The absolute haze production rates for the latter case were measured to rise from 0.01 mg hr^{-1} at 400 K to 0.013 mg hr^{-1} at 600 K. The ratio of 1.3 between these two values is tantalizingly close to the value of 1.35 we estimate for the ratio of photolysis rates, $J_{600\,K}/J_{400\,K}$, of a pure CO_2 gas at these two temperature limits (Venot et al. 2018), assuming the spectral density of the UV lamp (Figure 2). Given that CO_2 is the main gas component at this metallicity, it is logical to correlate the temperature dependence of the CO_2 cross section with the observed variation of the haze production. At lower metallicities, the contribution of CO_2 is smaller; therefore, its impact on the haze production is smaller. However, the reason for the inversion of the haze yield with temperature is not clear and has to be sought in the chemical pathways leading to the haze formation. Such an investigation necessitates a detailed comparison with the experiments at identical conditions (gas mixtures/energy input) to identify the role of each process on haze production, and which will further benefit from comparison with the experimentally derived gas-phase products (He et al. 2019). Such a study goes beyond our goals for the current investigation. However, the conclusion we derive from this comparison of relative production yields is that the theoretical simulations capture the qualitative behavior identified in the experiments and, vice versa, the experiments provide a picture of haze formation representative of theoretical anticipations, indicating promising results from this venue of investigation.

We now turn our attention to the implications of the haze particles on the atmosphere. We find that our simulated haze distributions (of either spherical or aggregate shape) do not impose major modifications to the radiation field at UV wavelengths and therefore do not have a major impact on the simulated chemical abundances. This occurs because, for the sub-Neptune conditions investigated here, gases provide a larger UV opacity than haze, under all metallicity conditions. For example, at solar metallicity conditions for which we can compare with previous evaluations for hot Jupiters (Lavvas & Koskinen 2017), H_2O, NH_3, and CH_4 have higher abundances for sub-Neptune conditions and therefore dominate the UV opacity.

On the contrary, at longer wavelengths where gas absorption decreases, haze opacity dominates. Thus, as with the case of hot Jupiter hazes, we find that the presence of such particles in the atmosphere could significantly affect the thermal structure. Our calculations show that absorption of stellar radiation by the particles results in the same energy deposition rate as for the main gas absorbers. For the 10,000× solar metallicity that is

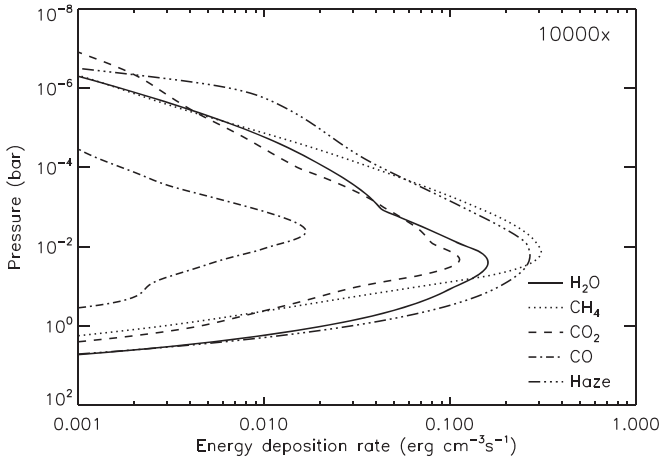

Figure 15. Energy deposition in the atmosphere of GJ 1214b from the absorption of stellar radiation. Here we compare the haze contribution with the main gaseous absorbers.

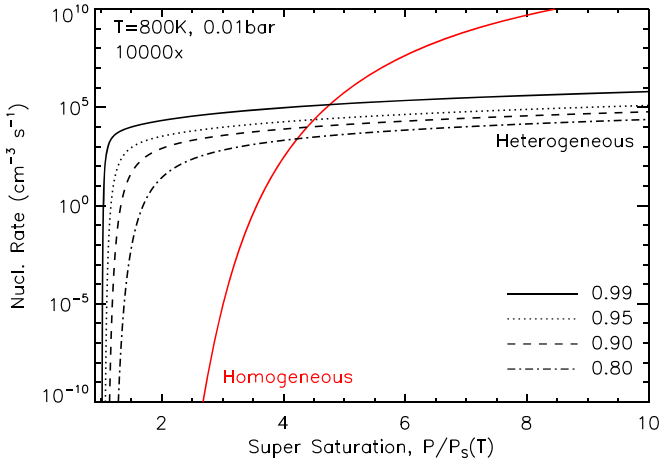

Figure 16. Homogeneous (red) and heterogeneous nucleation rates for KCl. For the heterogeneous rates we consider our simulated haze particle distribution (spheres) for the 10,000× solar metallicity case at 800 K and 0.01 bars. Different curves correspond to various values for the contact angle, θ, between the substrate (haze particle) and the condensed phase, expressed as $\mu = \cos(\theta)$.

closer to the observed spectra, CH_4 is the dominant gas absorber, followed by H_2O. Our calculations suggest that the haze contribution in the energy deposition is similar to that of CH_4 and at pressures lower than 0.1 mbars haze dominates over all gas contributions up to 1 μbar (Figure 15). Previous studies, focusing on the impact of cloud particles on the energy balance, found that they could significantly affect the atmospheric thermal structure (Charnay et al. 2015b; Roman & Rauscher 2019). Soot composition particles are expected to have a larger impact, as they demonstrate higher absorptivity than the cloud composition components. However, the extent of this impact will depend on how efficiently haze particles are consumed as condensation nuclei in cloud formation.

Our preliminary estimates for the impact of nucleation demonstrate that haze particles would efficiently act as nucleation sites. Our calculations for the condensation of KCl, which is expected to condense at higher altitudes compared to ZnS (see Figure 1 and Gao & Benneke 2018), demonstrate that haze particles would readily lead to the formation of cloud particles at very low supersaturations (Figure 16). Even for small values of the contact angle between

the haze particle and the condensed phase formed on its surface, a parameter that is currently unknown, the heterogeneous nucleation rate dominates over the homogeneous nucleation rate at low supersaturations. Currently in the simulations of cloud formation in mini-Neptunes/super-Earths (Gao & Benneke 2018; Ohno & Okuzumi 2018) KCl condensation is assumed to start through homogeneous nucleation, while ZnS is formed heterogeneously on the surface of the KCl cloud particles. Thus, the different population of nucleation sites imposed by the presence of the photochemical hazes will have implications for the properties of all subsequent cloud particle distributions. Therefore, our results demonstrate that a coupled picture between photochemical hazes and cloud formation is necessary.

Our simulations provide a disk-average picture of haze properties for the atmosphere of GJ 1214b, which will be further modulated by the atmospheric circulation. Although the assumed K_{ZZ} profile in our study does take into consideration the impact of advection on the vertical direction, horizontal redistribution of the hazes may further modify their impact on the energy deposition, as well as their transit signature (Line & Parmentier 2016). Previous studies have mainly focused on the impact of temperature changes on the properties of clouds, but studies with passive tracers in GCM (more consistent with what should be anticipated for haze particles) demonstrate that circulation can result in significant inhomogeneity in the particle distribution across the planetary terminator (Parmentier et al. 2013; Charnay et al. 2015a). Moreover, horizontal modifications of the chemical composition may further affect the local haze production, which we assumed here to be dominated by the dayside production rate. Finally, modification of the atmospheric properties along the line of sight of transit observations can modify the observed planet radius (Caldas et al. 2019). Although such an effect appears to be smaller for sub-Neptune planets relative to hot Jupiters, it has to be evaluated for each case. Proper evaluation of these processes requires a detailed treatment of the atmospheric 3D properties with a coupled model of circulation, photochemistry, and microphysics. Our present work can serve as a starting point for such an endeavor.

8. Conclusions

Our study reveals the properties of photochemical hazes in atmospheres of super-Earth and mini-Neptune atmospheres, focusing on the case of GJ 1214b. We find that photochemical haze formation with a formation efficiency of 10% relative to the photolytically produced mass fluxes provides haze particle distributions consistent with the observed transit spectrum when high-metallicity conditions are considered (10,000× solar). We discuss the properties of both spherical and aggregate particles and demonstrate that the two growth mechanisms lead to different particle size distributions but to similar transit signatures when the fractal aggregate dimension is 2. We also find that the presence of photochemical hazes can have major ramifications for the properties of the condensation cloud particles and that a coupled description including both heterogeneous components should provide a more realistic picture for the properties of heterogeneous compounds in such atmospheres, as well as for their implications on the thermal structure.

In a broader sense we find that increasing the atmospheric metallicity can result in nonmonotonic changes in the haze production rate, although the differences in the estimated rates are small (factor of ∼3) relative to the range of metallicity cases considered (1×−10,000× solar). To a first degree explored here we find that these modifications depend on the complex interplay between the dominant gaseous abundances for each metallicity case and their interaction with the incoming stellar radiation. Comparison of our simulations with laboratory experiments of photochemical haze production reveals a qualitatively consistent picture. On a second degree further variations will be imposed by changes on the chemical pathways leading to haze formation that are currently unknown, and which will define the absolute haze formation yield. These are aspects that need to be investigated in the future through combined theoretical and experimental approaches under well-constrained conditions.

We thank Prof. P. Rannou for his comments on the impact of D_f on the aggregate optical properties. This work was supported by the Programme National de Planétologie (PNP) of CNRS/INSU, cofunded by CNES. M.S. was supported by NASA Headquarters under the NASA Earth and Space Science Fellowship Program—grant 80NSSC18K1248. A.G.M. acknowledges the support of the DFG priority program SPP 1992 "Exploring the Diversity of Extrasolar Planets (GA 2557/1-1).

ORCID iDs

Panayotis Lavvas https://orcid.org/0000-0002-5360-3660
Maria E. Steinrueck https://orcid.org/0000-0001-8342-1895
Antonio García Muñoz https://orcid.org/0000-0003-1756-4825

References

Adams, D., Gao, P., de Pater, I., & Morley, C. V. 2019, ApJ, 874, 61
Angerhausen, D., Dreyer, C., Placek, B., et al. 2017, A&A, 608, A120
Barstow, J. K., Aigrain, S., Irwin, P. G. J., & Sing, D. K. 2017, ApJ, 834, 50
Cabane, M., Rannou, P., Chassefiere, E., & Israel, G. 1993, P&SS, 41, 257
Caldas, A., Leconte, J., Selsis, F., et al. 2019, A&A, 623, A161
Charnay, B., Meadows, V., & Leconte, J. 2015a, ApJ, 813, 15
Charnay, B., Meadows, V., Misra, A., Leconte, J., & Arney, G. 2015b, ApJL, 813, L1
Crossfield, I. J. M., & Kreidberg, L. 2017, AJ, 154, 261
Fontenla, J. M., Linsky, J. L., Witbrod, J., et al. 2016, ApJ, 830, 1
Fraine, J. D., Deming, D., Gillon, M., et al. 2013, ApJ, 765, 127
France, K., Loyd, R. O. P., Youngblood, A., et al. 2016, ApJ, 820, 1
Gao, P., & Benneke, B. 2018, ApJ, 863, 165
Gao, P., Marley, M. S., Zahnle, K., Robinson, T. D., & Lewis, N. K. 2017, AJ, 153, 139
García Muñoz, A. 2007, P&SS, 55, 1426
García Muñoz, A. 2018, ApJ, 854, 108
García Muñoz, A., & Cabrera, J. 2018, MNRAS, 473, 1801
García Muñoz, A., Lavvas, P., & West, R. A. 2017, NatAs, 1, 0114
Gladstone, G. R., Stern, S. A., Ennico, K., et al. 2016, Sci, 351, aad8866
He, C., Hörst, S. M., Lewis, N. K., et al. 2018, AJ, 156, 38
He, C., Hörst, S. M., Lewis, N. K., et al. 2019, ESC, 3, 39
Hörst, S. M., He, C., Lewis, N. K., et al. 2018, NatAs, 2, 303
Hörst, S. M., & Tolbert, M. A. 2013, ApJL, 770, L10
Kataria, T., Showman, A. P., Fortney, J. J., Marley, M. S., & Freedman, R. S. 2014, ApJ, 785, 92
Kawashima, Y., & Ikoma, M. 2018, ApJ, 853, 7
Koskinen, T. T., Harris, M. J., Yelle, R. V., & Lavvas, P. 2013, Icar, 226, 1678
Krasnopolsky, V. A., & Cruikshank, D. P. 1995, JGR, 100, 21271
Kreidberg, L., Bean, J. L., Désert, J.-M., et al. 2014, Natur, 505, 69
Lavvas, P., Galand, M., Yelle, R. V., et al. 2011a, Icar, 213, 233
Lavvas, P., & Koskinen, T. 2017, ApJ, 847, 32
Lavvas, P., Koskinen, T., & Yelle, R. V. 2014, ApJ, 796, 15
Lavvas, P., Sander, M., Kraft, M., & Imanaka, H. 2011b, ApJ, 728, 80

Lavvas, P., Yelle, R. V., & Griffith, C. A. 2010, Icar, 210, 832
Lavvas, P., Yelle, R. V., Koskinen, T., et al. 2013, PNAS, 110, 2729
Lee, G., Helling, C., Dobbs-Dixon, I., & Juncher, D. 2015, A&A, 580, A12
Line, M. R., & Parmentier, V. 2016, ApJ, 820, 78
Linsky, J. L., Fontenla, J., & France, K. 2014, ApJ, 780, 61
Lopez, E. D., & Fortney, J. J. 2014, ApJ, 792, 1
Loyd, R. O. P., France, K., Youngblood, A., et al. 2016, ApJ, 824, 1
Lozovsky, M., Helled, R., Dorn, C., & Venturini, J. 2018, ApJ, 866, 49
Mallonn, M., Herrero, E., Juvan, I. G., et al. 2018, A&A, 614, A35
Marley, M. S., Ackerman, A. S., Cuzzi, J. N., & Kitzmann, D. 2013, in Comparative Climatology of Terrestrial Planets, ed. S. J. Mackwell et al. (Tucson, AZ: Univ. Arizona Press), 367
McBride, B. J., Zehe, M. J., & Gordon, S. 2002, NASA Glenn Coefficients for Calculating Thermodynamic Properties of Individual Species, Technical Report, NASA TP-2002-211556, NASA
Miller-Ricci Kempton, E., Zahnle, K., & Fortney, J. J. 2012, ApJ, 745, 3
Morley, C. V., Fortney, J. J., Kempton, E. M. R., et al. 2013, ApJ, 775, 33
Morley, C. V., Fortney, J. J., Marley, M. S., et al. 2012, ApJ, 756, 172
Morley, C. V., Fortney, J. J., Marley, M. S., et al. 2015, ApJ, 815, 110
Moses, J. I., Line, M. R., Visscher, C., et al. 2013, ApJ, 777, 34
Moses, J. I., Visscher, C., Fortney, J. J., et al. 2011, ApJ, 737, 15
Narita, N., Fukui, A., Ikoma, M., et al. 2013, ApJ, 773, 144
Nascimbeni, V., Mallonn, M., Scandariato, G., et al. 2015, A&A, 579, A113
Ohno, K., & Okuzumi, S. 2018, ApJ, 859, 34
Parmentier, V., Showman, A. P., & Lian, Y. 2013, A&A, 558, A91
Poling, B. E., Prausnitz, J. M., & O'Connell, J. P. 2001, The Properties of Gases and Liquids (New York: McGraw-Hill),
Powell, D., Zhang, X., Gao, P., & Parmentier, V. 2018, ApJ, 860, 18
Pruppacher, H. R., & Klett, J. D. 1978, Microphysics of Clouds and Precipitation (Dordrecht: Reidel)
Rackham, B., Espinoza, N., Apai, D., et al. 2017, ApJ, 834, 1
Rannou, P., Cabane, M., Botet, R., & Chassefière, E. 1997, JGR, 102, 10997
Rannou, P., Cours, T., Le Mouélic, S., et al. 2010, Icar, 208, 850
Rannou, P., Toledo, D., Lavvas, P., et al. 2016, Icar, 270, 291
Robinson, T. D., Fortney, J. J., & Hubbard, W. B. 2017, ApJ, 850, 128
Roman, M., & Rauscher, E. 2019, ApJ, 872, 1
Seignovert, B., Rannou, P., Lavvas, P., Cours, T., & West, R. A. 2017, Icar, 292, 13
Sing, D. K., Fortney, J. J., Nikolov, N., et al. 2016, Natur, 529, 59
Tomasko, M. G., Doose, L., Engel, S., et al. 2008, P&SS, 56, 669
Tomasko, M. G., Doose, L. R., Dafoe, L. E., & See, C. 2009, Icar, 204, 271
Venot, O., Benilan, Y., Fray, N., et al. 2018, A&A, 609, A34
West, R. A., Lavvas, P., Anderson, C., & Imanaka, H. 2014, in Titan Interior, Surface, Atmosphere and Space Environment, ed. I. Müller-Wodarg et al. (Cambridge: Cambridge Univ. Press)
Youngblood, A., France, K., Loyd, R. O. P., et al. 2016, ApJ, 824, 1
Zahnle, K., Marley, M. S., Morley, C. V., & Moses, J. I. 2016, ApJ, 824, 137